Global Biogeochemical Cycles

RESEARCH ARTICLE
10.1029/2024GB008373

Stable Iron Isotopes Constrain the Sedimentary Input of Dissolved Iron to the Ocean

Ying Ye[1] and **Christoph Völker**[1]

[1]Alfred-Wegener-Institut Helmholtz-Zentrum für Polar- und Meeresforschung (AWI), Bremerhaven, Germany

Key Points:

- An ocean box model has been developed to describe the marine cycle of iron and its stable isotopes
- Model-data comparisons reveal the necessity to consider spatially distinct isotopic signals and fractionation processes in seawater
- The global sedimentary source is constrained between 7.5−15 Gmol Fe yr^{-1} which will be further explored in full ocean biogeochemistry models

Supporting Information:

Supporting Information may be found in the online version of this article.

Correspondence to:

Y. Ye,
Ying.Ye@awi.de

Citation:

Ye, Y., & Völker, C. (2025). Stable iron isotopes constrain the sedimentary input of dissolved iron to the ocean. *Global Biogeochemical Cycles*, *39*, e2024GB008373. https://doi.org/10.1029/2024GB008373

Received 27 SEP 2024
Accepted 25 APR 2025

Author Contributions:

Conceptualization: Ying Ye, Christoph Völker
Formal analysis: Ying Ye
Funding acquisition: Ying Ye
Investigation: Ying Ye
Methodology: Ying Ye, Christoph Völker
Project administration: Ying Ye
Software: Ying Ye, Christoph Völker
Supervision: Ying Ye
Validation: Ying Ye
Visualization: Ying Ye
Writing – original draft: Ying Ye, Christoph Völker

Abstract Iron is a key micronutrient for marine biota and potentially one of the main drivers of ocean feedback to changing climate. There is however no consensus on the relative role of different external iron sources to the ocean, hampering our ability to predict how the oceanic iron cycle and biological carbon pump will react to climate change. For the last two decades, stable iron isotopes have been increasingly used in field studies to track contributions of different iron sources and modeling studies started to help interpreting isotope observations. However, measured isotopic compositions of iron sources can vary substantially, and the isotopic signatures of different sources can overlap, leading to high uncertainty in constraining the magnitude of the sources. This study aims to examine the sensitivity of seawater iron isotopes to the uncertainty in the sedimentary source. An existing box model of the marine carbon cycle is extended with a description of the cycle of iron and its stable isotopes. Experiments have been done with variable isotopic end-member signature and strength of the sedimentary source, and fractionation through biological uptake and binding to organic ligands. The model results reveal the necessity to consider spatially distinct isotopic end-member signatures for the sedimentary source and fractionations so as to reproduce observed spatial gradients of seawater iron isotopic composition. By assuming a sedimentary input of 7.5–15 Gmol Fe yr^{-1}, the model is able to reproduce observed concentrations of dissolved iron and its isotopes in large ocean regions, providing useful constraints for complex global biogeochemistry models.

Plain Language Summary Iron is essential for marine life and plays a key role in how oceans respond to climate change. However, scientists are still unsure about the relative importance of different sources of iron to the ocean, making it difficult to predict how the iron supply and biological activity in the ocean to store carbon will change with climate. Over the past 20 years, researchers have used iron isotopes to track these sources, but overlapping and variable isotope signatures create uncertainty. This study used a box model to explore how uncertainties in iron and iron isotopes from sediments affect seawater iron isotopes, and to make a first-order estimate of the global sedimentary input of iron. The simple box model matches observed iron levels and isotope compositions in the main ocean regions with a sediment input of iron of 7.5–15 Gmol per year, offering insights for more complex global models.

1. Introduction

Iron is an essential micronutrient for ocean biota, and its distribution strongly affects the magnitude of primary productivity and with it the carbon uptake in the ocean. While we are slowly obtaining a picture of the present global distribution of dissolved iron (DFe) in the ocean, there is still no consensus on the mechanisms behind this distribution, especially on the relative role of different external iron sources to the ocean. The main sources of iron for the open ocean include dust deposition (Duce & Tindale, 1991), marine sediments (Elrod et al., 2004), rivers (de Baar & de Jong, 2001) and hydrothermal vents (Elderfield & Schultz, 1996; Tagliabue et al., 2010). A number of other sources are also known and may be important locally, for example, volcanic ash (Hamme et al., 2010), non-lithogenic aerosol deposition, for example, from biomass burning (Guieu et al., 2005), submarine groundwater discharge (Windom et al., 2006), icebergs (Raiswell, 2011), sea ice (Lannuzel et al., 2010), and subglacial meltwaters (Gerringa et al., 2012). Several sources are also altered by human activities, for example, shipboard aerosols, which both act as direct iron input and alter iron solubility in bulk aerosols (Hamilton et al., 2020; Ito, 2013).

There is still considerable uncertainty in the estimates of all external iron sources to the ocean, and some of the flux estimates may not be mutually exclusive, for example, iron from glacial runoff or icebergs can be double counted as sedimentary input, if it is released from particles only after deposition on the sea floor. The largest uncertainty concerns one of the largest fluxes, namely sediment input, for which estimates vary by several orders

of magnitude. This uncertainty is reflected also in present models of the iron cycle in their different assumptions on iron sources (Somes et al., 2021; Tagliabue et al., 2016). While all models are tuned by changing the loss processes of iron, for example, through scavenging, that is, adsorption onto particles, to arrive at iron concentrations comparable to observations, the resulting residence times of iron vary over one order of magnitude between models, which substantially limits our understanding of the marine cycle of iron. Moreover, some of the external sources of iron (e.g., dust and riverine input) are predicted to change strongly with ongoing climate change (Kohfeld & Ridgwell, 2009; Martínez-García et al., 2014; Robinson et al., 2014; Wehrmann et al., 2014), while others might not (e.g., hydrothermal vents). The uncertainty of how relevant the specific sources are, is therefore severely hampering our ability to prognose how the oceanic iron cycle and biological carbon pump will react to climate change.

For the last two decades, stable isotopes of iron have been used to identify the relative contribution of different sources of iron to the ocean. This is based on observations that the external iron sources differ in their stable isotope compositions, the end-member signatures as they enter seawater, which contain information on their origins and history. Recent analytical advances enable resolving variations in the isotopic end-member of iron sources and of iron in seawater, which can in principle be used to infer the relative contribution of different iron sources. Iron has four naturally occurring stable isotopes:^{54} Fe (5.85%), ^{56}Fe (91.75%), ^{57}Fe (2.12%) and ^{58}Fe (0.28%). Iron isotopic composition is commonly reported in terms of the ratio between the two most abundant iron isotopes (^{56}Fe/^{54}Fe), and measured using Multi-Collector-Inductively Coupled Plasma-Mass Spectrometry (MC-ICP-MS). The δ^{56}Fe value is determined by normalizing the isotope ratio in samples to the ratio of the IRMM-014 reference standard (Dauphas et al., 2017):

$$\delta^{56}\mathrm{Fe} = \left(\frac{{}^{56}\mathrm{Fe}/{}^{55}\mathrm{Fe}_{\mathrm{sample}}}{{}^{56}\mathrm{Fe}/{}^{54}\mathrm{Fe}_{\mathrm{standard}}} - 1 \right) \cdot 10^{3} \quad (1)$$

Generally in marine environments, δ^{56}Fe varies in a range of ∼4‰, with marine sedimentary rocks and bulk aerosols at ∼0‰ and lighter isotopic signatures in DFe influenced by redox chemistry (e.g., in hydrothermal vent fluids and reducing sediment pore waters) (Beard & Johnson, 2004). A number of studies give detailed iron isotope signatures from hydrothermal vents (Beard et al., 2003; Bennett et al., 2009; Severmann et al., 2004), sedimentary source (e.g., Henkel et al., 2016; Homoky et al., 2009, 2013; John et al., 2012; Severmann et al., 2010), aerosol input (Beard et al., 2003; Mead et al., 2013; Waeles et al., 2007), and riverine input (e.g., Bergquist & Boyle, 2006; Escoube et al., 2009, 2015). Based on this knowledge of source end-member signatures, some regional studies attempted to discriminate between iron from different sources from observed seawater δ^{56}Fe (e.g., John & Adkins, 2012; Labatut et al., 2014; Radic et al., 2011) and similar mass balance approaches were also applied to quantify contributions of different iron sources to one North Atlantic section (Conway & John, 2014). Assuming two dominant iron sources for each defined region, Conway and John (2014) made estimations of the contribution of each single source in the region by considering the physical mixing of the two sources with their unique end-member compositions, the so-called "two-component mixing" method.

Using stable isotopes to trace iron sources in natural systems, however, has shown some limitations. One obvious problem with the "two-component mixing" method is that with just one isotope measurement only two sources can be discriminated, so assumptions have to be made which two sources are dominant. Further, the end-member signatures of some iron sources can hardly be distinguished from each other (e.g., dust with ∼0.1‰ and riverine input with a range from −0.6 to +0.4‰); while in seawater, the isotope signatures of DFe is additionally changed by fractionating processes such as redox reactions, solid–solute reactions, and ligand stabilization reactions, both in their formation regions (e.g., dust source and subsequent atmospheric processing) and during their introduction into seawater (e.g., dust solubilization in surface waters) (Fitzsimmons & Conway, 2023). For example, binding with organic ligands stabilizes DFe against hydrolysis and precipitation and allows its concentrations to exceed inorganic solubility limitations (Hunter & Boyd, 2007; Liu & Millero, 2002). Here, heavy isotope enrichment has been observed in organically complexed species compared with free aqueous species of iron (e.g., Dideriksen et al., 2008; Morgan et al., 2010). Biological uptake by phytoplankton can also contribute to iron isotope fractionation, leading to enrichment of heavier isotopes in surface seawater (Ellwood et al., 2015). One clear indication for the contribution of fractionation processes is that the observed seawater δ^{56}Fe is mostly heavier than its sources (e.g., Conway & John, 2014; Conway & John, 2015; Radic et al., 2011). Therefore, a modeled system

considering both different end-member signatures of iron sources, fractionation processes and physical mixing of isotopic signals can certainly help to explain observations of iron isotopes (e.g., König et al., 2021; König et al., 2022).

Well-defined source end-members are the prerequisites for both the two-component mixing method and modeling studies. However, end-member signatures of some iron sources have been reported with large variations and even different signs have been found for the sedimentary iron source (Homoky et al., 2009, 2013; Klar et al., 2017; Severmann et al., 2006). Microbial dissimilatory iron reduction (DIR) is a common process driving the iron dissolution from marine sediments and results in an enrichment of the lighter isotope in aqueous ferrous iron and thus a relatively strong negative δ^{56}Fe in benthic iron flux ($-0.9‰$ to $-3.3‰$) (e.g., Beard et al., 2003; Crosby et al., 2005, 2007; Severmann et al., 2006). Measurements of benthic iron fluxes have shown that DIR could be the dominant iron source to the coastal ocean and beyond (e.g., Elrod et al., 2004; Severmann et al., 2010). Consistent with a strong role of reductive processes, Elrod et al. (2004) found a clear correlation between the iron flux from sediments and the oxidation rate of organic matter. Another process, non-reductive dissolution, observed in oxygenated sediments and often related to sediment resuspension, has been proposed to have the opposite effect on δ^{56}Fe and cause the enrichment of the heavier isotope in DFe pool and a slightly positive δ^{56}Fe ($+0.4‰$) of the sedimentary iron source (e.g., Homoky et al., 2013; Radic et al., 2011). Furthermore, some studies suggest that production of iron colloids from lithogenic weathering fuels sedimentary iron supply away from low-oxygen systems, with a nearly neutral isotopic signature of $+0.07 \pm 0.07‰$ (e.g., Homoky et al., 2021). Thus, various source end-member signatures of the sedimentary iron have been reported between the DIR and non-reductive source and factors controlling its variations are still uncertain (Homoky et al., 2016). Henkel et al. (2018) pointed out that multifold factors are involved in altering iron isotopic compositions in pore water, including the amount of reducible Fe oxides and organic matter, the isotopic composition of the primary and secondary ferric substrates, sedimentation rates, and physical reworking (bioturbation, ice scraping). Therefore, how sensitive the seawater δ^{56}Fe is to these variations in the sedimentary iron source is crucial for our attempt to use iron isotopes to constrain the ocean iron sources and the residence time of iron.

In this study, we investigated the sensitivity of the isotopic composition of seawater DFe to the isotopic composition and strength of sedimentary input into the ocean. The marine cycles of iron and stable iron isotopes were described in an ocean box model, considering three external iron sources (dust, sediment and hydrothermal vents), and biological uptake and organic complexation as fractionation processes. The isotopic signal of the sedimentary iron input was varied in sensitivity experiments to represent the DIR and/or non-reductive source. In addition, the sedimentary flux of iron was varied over two orders of magnitude (which is approximately the range used in different global ocean biogeochemical models), while keeping the iron concentrations in each ocean box close to observations by co-varying the rate of scavenging loss of iron. With the three distinct ocean boxes, the model is able to roughly estimate contributions of different iron sources to the large ocean regions, allowing us to investigate and give hints whether the sedimentary input of iron can be constrained with the help of the available measurements of iron isotopic composition despite the uncertainty in end-member signatures of iron sources.

2. Methods

2.1. Model of Fe

In this study we used the box model of the ocean carbon cycle (Figure 1) originally developed by Sarmiento and Toggweiler (1984), extending the model with a description of the ocean iron cycle. The ocean is divided into three boxes: the low-latitude surface box (Box_L), the high-latitude surface box (Box_H) and the deep-ocean box (Box_D). Box_L is 100 m thick and covers the surface area between 50°N and 50°S, roughly about 85% of the total ocean surface area; Box_H has a thickness of 250 m and covers the high-latitude regions north of 50°N and south of 50°S. Exchange between the ocean boxes includes the thermohaline overturning, mixing at the high latitudes and sinking of organic particles from the two surface boxes into the deep-ocean box. The volumes and exchange fluxes are taken from Sarmiento and Toggweiler (1984).

The iron model considers three external sources of DFe namely dust deposition, hydrothermal vents and marine sediments. The input of DFe into each box was prescribed based on a previous and more complex box model of the marine iron cycle (Völker & Ye, 2022). The input fluxes from different sources are listed in Table 1 for the reference experiment, together with the volumes of each box.

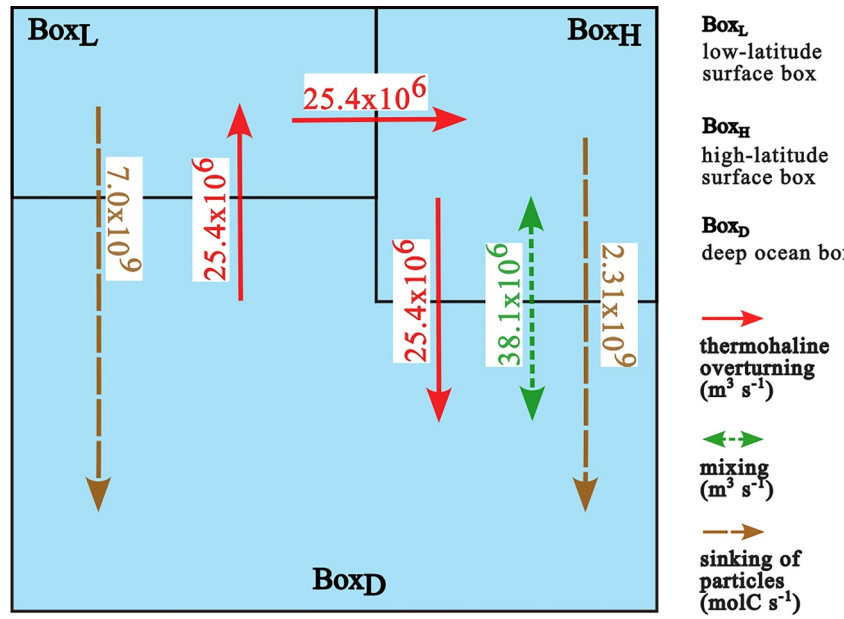

Figure 1. The ocean box model and fluxes between the boxes used in this study. The thickness of Box_L and Box_H are 100 and 250 m, respectively, and the volumes of the three boxes are given in Table 1.

DFe in seawater is consumed by photosynthetic production of organic biomass and recycled by degradation of organic material. Both processes are represented in the model proportional to carbon consumption and release, assuming a ratio of 1 μmol m^{-3} Fe: 200 mmol m^{-3} C (Table 2), a typical value obtained from radiolabeled phytoplankton uptake experiments (King et al., 2012). DFe is consumed in the two surface boxes and remineralized in the deep ocean box. The rate of change of DFe in each box is calculated considering the biological processes, exchange between ocean boxes and the removal by particle adsorption. Free iron (Fe'), that is, not bound by organic ligands, is scavenged by sinking particles. As concentrations of sinking particles can not be represented adequately in a simple box model, we make the assumption that the effective rate of scavenging is 100 times as high in the surface boxes as in the deep ocean box. The fraction of Fe' in DFe is calculated by assuming a constant concentration of organic ligands of 1 μmol m^{-3} (Table 2). An example of calculating Fe' in Box_L (Fe'_L) is given in Equation 5.

Table 1
Properties of the Ocean Boxes and the External Sources of Iron

Box	Volume (m^3)	Iron source	Input (mol Fe $year^{-1}$)
Box_L	3.06×10^{16}	Dust	8.2×10^8
		Hydrothermal vents	4.5×10^4
		Sediments	1.7×10^8
Box_H	1.35×10^{16}	Hydrothermal vents	5.5×10^5
		Sediments	1.4×10^8
Box_D	1.32×10^{18}	Hydrothermal vents	8.5×10^8
		Sediments	4.4×10^8

Note. Dust and hydrothermal source of iron are kept identical between model experiments, while only the reference sedimentary input is listed in the table (referred to as "1X" in figures).

The equations for DFe in each box are

$$\frac{d}{dt}\mathrm{DFe}_L = \frac{1}{V_L}(\mathrm{Tr}\cdot(\mathrm{DFe}_D - \mathrm{DFe}_L) - P_L \cdot r_{\mathrm{Fe2C}} + S_L) - R_L \quad (2)$$

$$\frac{d}{dt}\mathrm{DFe}_H = \frac{1}{V_H}(\mathrm{Tr}\cdot(\mathrm{DFe}_L - \mathrm{DFe}_H) + M\cdot(\mathrm{DFe}_D - \mathrm{DFe}_H) - P_H \cdot r_{\mathrm{Fe2C}} + S_H) - R_H \quad (3)$$

$$\frac{d}{dt}\mathrm{DFe}_D = \frac{1}{V_D}(\mathrm{Tr}\cdot(\mathrm{DFe}_H - \mathrm{DFe}_D) - M\cdot(\mathrm{DFe}_D - \mathrm{DFe}_H) + (P_L + P_H)\cdot r_{\mathrm{Fe2C}} + S_D) - R_D \quad (4)$$

where DFe stands for the dissolved iron concentration, and the subscripts $_{L,H,D}$ represent the three model boxes. V is the volume of a specific box, Tr the total volume flow from one to another box through overturning (red arrows in Figure 1) and M the total volume flow due to high-latitude

Table 2
Parameters Used in the Box Model

Symbol	Description	Unit	Value	References
$\delta^{56}Fe_{dust}$	δ^{56}Fe of dust	‰	+0.10	A, B
$\delta^{56}Fe_{hydro}$	δ^{56}Fe of hydrothermal vents	‰	−0.50	C, D, E
$\delta^{56}Fe_{sed}$	δ^{56}Fe of reductive sediments	‰	−3.00	F
$\delta^{56}Fe_{nonsed}$	δ^{56}Fe of non-reductive sediments	‰	+0.30	G, H, I
r_{Fe2C}	Fe to C ratio in biomass	µmol:mmol	1:200	L
r_{scav}	Scavenging rate constant	day^{-1}	min. 0.055	
			max. 3.2	
K_{cond}	Conditional stability constant	$\mu mol^{-1}\ m^3$	200	
Lig	Ligand concentration	$\mu mol\ m^{-3}$	1.0	
α_{upt}	Fractionation factor by biological uptake		+0.99974	J
α_{comp}	Fractionation factor by organic complexation		+1.0001	K

Note. A: Waeles et al. (2007); B: Chen et al. (2020); C: Rouxel et al. (2008); D: Bennett et al. (2009); E: Nasemann et al. (2018); F: Severmann et al. (2010); G: Radic et al. (2011); H: Homoky et al. (2013); I: Scholz et al. (2014); J: Ellwood et al. (2015); K: sensitivity studies based on Dideriksen et al. (2008); L: King et al. (2012).

mixing (the green arrow in Figure 1). The term P describes the biological carbon fixation into biomass and thus is a removal of iron from the surface boxes and a gain in the deep box which is calculated from the carbon flux to iron flux with r_{Fe2C}, the Fe:C ratio mentioned above. S stands for the sum of iron input from all external sources and R the removal of iron by particle scavenging. The latter is calculated from the free iron (Fe') concentration in each box and a constant scavenging rate which is 100-fold higher in the surface boxes than in the deep ocean box. An example of calculating the scavenging loss of DFe_L is given in Equation 5 and the scavenging loss of DFe_D is calculated using $r_{scav}/100$.

$$\begin{aligned} R_L &= r_{scav} \cdot Fe'_L \\ A &= \frac{Lig - DFe_L + K_{cond}}{2} \\ Fe'_L &= -A + \sqrt{DFe_L \cdot K_{cond} + A^2} \end{aligned} \tag{5}$$

2.2. Model of ^{56}Fe

The cycle of ^{56}Fe in DFe $\left(DFe^{56}\right)$ is described in an analogous way to DFe in the model, but with additional processes changing DFe^{56} concentrations, the so-called "fractionation". Considering fractionation by biological uptake and organic complexation with ligands, the equations of DFe^{56} in each box look like:

$$\frac{d}{dt}DFe_L^{56} = \frac{1}{V_L}\left(Tr \cdot \left(DFe_D^{56} - DFe_L^{56}\right) - P_L \cdot r_{Fe2C} \cdot r_L^{56} \cdot \alpha_{upt} + S_L^{56}\right) - \frac{R_L \cdot r_L^{56}}{\alpha_{comp}} \tag{6}$$

$$\frac{d}{dt}DFe_H^{56} = \frac{1}{V_H}\left(Tr \cdot \left(DFe_L^{56} - DFe_H^{56}\right) + M \cdot \left(DFe_D^{56} - DFe_H^{56}\right) - P_H \cdot r_{Fe2C} \cdot r_H^{56} \cdot \alpha_{upt} + S_H^{56}\right) - \frac{R_H \cdot r_H^{56}}{\alpha_{comp}} \tag{7}$$

$$\begin{aligned} \frac{d}{dt}DFe_D^{56} = \frac{1}{V_D}\Big(&Tr \cdot \left(DFe_H^{56} - DFe_D^{56}\right) - M \cdot \left(DFe_D^{56} - DFe_H^{56}\right) + \left(P_L \cdot r_{Fe2C} \cdot r_L^{56} + P_H \cdot r_{Fe2C} \cdot r_H^{56}\right) \\ &\cdot \alpha_{upt} + S_D^{56}\Big) - \frac{R_D \cdot r_D^{56}}{\alpha_{comp}} \end{aligned} \tag{8}$$

The superscript ^{56} denotes the concentration of ^{56}Fe (e.g., DFe_L^{56}), the ratio of ^{56}Fe to total DFe (e.g., r_L^{56}) or the external source of ^{56}Fe (e.g., S_L^{56}) in each ocean box. Fractionation by biological uptake and organic complexation

are taken into account through α_{upt} and α_{comp}, respectively. The inverse of α_{comp} is considered for the fractionation by scavenging since Fe that is not bound to organic ligands undergoes scavenging. Details of parameter choices are given below.

The model simulates the concentrations of dissolved ^{56}Fe $\left(DFe^{56}\right)$ and the sum of all Fe isotopes (DFe). For comparison with observed δ^{56}Fe (defined as Equation 1) we therefore have to calculate δ^{56}Fe out of the ratio between modeled DFe^{56} and total DFe concentration, r^{56}, from:

$$\delta^{56}\mathrm{Fe} = \frac{r^{56}\left(1 + r^{56}_{std} + r^{57}_{std} + r^{58}_{std}\right) - r^{56}_{std}}{r^{56}_{std} - r^{56}\left(r^{56}_{std} + 3r^{57}_{std}/2 + 2r^{58}_{std}\right)}, \tag{9}$$

where r^{56}_{std}, r^{57}_{std} and r^{58}_{std} are reference isotopic ratios of ^{56}Fe, ^{57}Fe and ^{58}Fe to ^{54}Fe, respectively. This relation is derived in the appendix (Section Appendix A) under the assumption of mass-dependent fractionation for the different iron isotopes (e.g., Dauphas et al., 2017).

2.2.1. Isotopic End-Member Signatures of Fe Sources

A ^{56}Fe fraction of 0.917517 is applied in the model as the initial value of $^{56}Fe_{DFe}$ in all three ocean boxes, corresponding to the value of the reference material IRMM-014 with a δ^{56}Fe of 0‰ (Dauphas et al., 2017). The three considered external sources in our model have isotopic compositions that significantly differ from this average ratio and the corresponding references are given in Table 2.

The measured end-member composition of dust varies between $0‰ \sim +0.3‰$(Abadie et al., 2017; Chen et al., 2020; Waeles et al., 2007); that of hydrothermal source exhibits a larger range from $-1‰$ to $-0.1‰$ (Bennett et al., 2009; Nasemann et al., 2018; Severmann et al., 2004); and the largest variability is found in sedimentary sources from the strongly light reductive signatures around $-3‰ \sim -1‰$ (Abadie et al., 2017; Conway & John, 2014; Severmann et al., 2010), to the slightly positive values (up to $+0.4‰$) of DIR sources (Conway & John, 2014; Homoky et al., 2013; Klar et al., 2017; Radic et al., 2011; Scholz et al., 2014) which are close that of the dust source. A set of sensitivity experiments were conducted (Table S1 in Supporting Information S1) to examine how the variability in the measured isotopic compositions of source end-members affects the isotopic composition in seawater. The source end-member compositions used in the standard experiments represent roughly the averages of the measurements.

2.2.2. Fractionation by Biological Uptake

Differences of δ^{56}Fe between particulate Fe (PFe) and DFe in the euphotic zone have been reported to be in the range of $-0.13‰$ to $-1‰$ in field studies (Ellwood et al., 2015, 2020; Radic et al., 2011; Sieber et al., 2021). Ellwood et al. (2015) found a time-dependent change in δ^{56}Fe of DFe and PFe across stages associated with the progression of the annual spring bloom: while DFe is isotopically lighter than or similar to PFe during the winter mixing and the onset of spring blooms, at the peak of blooms δ^{56}Fe of PFe is significantly lighter than in the dissolved iron pool ($\Delta\delta^{56}Fe_{PFe-DFe} = -0.26‰$), demonstrating the maximal effect of isotopic fractionation by biological uptake. Therefore, we assumed in this study that biological uptake changes δ^{56}Fe by 0.99974 (i.e., $1-0.26‰$).

2.2.3. Fractionation by Organic Complexation

A fractionation of 0.6‰ was measured in the laboratory experiments between inorganic Fe(III) and Fe(III)-ligand complexes with a strong model ligand DFOB (desferrioxamine B) (Dideriksen et al., 2008). A strong positive correlation between fractionation factors and the iron-binding affinity of ligands have been found by (Morgan et al., 2010). We conducted sensitivity simulations by varying the fractionation by organic complexation between ±100% from 0.6‰ and found better model-data matches with weaker fractionations, indicating that most of natural ligands might have lower iron-binding affinities than DFOB. Results of some tuning experiments are shown in (Table S1 and Figure S8 in Supporting Information S1). Therefore, we assumed that iron bound with ligands becomes isotopically 0.1‰ heavier than Fe'; scavenging only removes the lighter Fe' and thus changes the isotopic composition of total DFe by $-\frac{1}{1.0001}$ (Equations 6–8, Table 2).

Table 3
Experimental Groups in This Study

Exp.	Sedimentary δ^{56}Fe (‰)	$Fract_{bio}$	$Fract_{compl}$
R_r	−3.0	No	No
R_{rb}	−3.0	Yes	No
R_{rbc}	−3.0	Yes	Yes
R_{nr}	+0.3	No	No
R_{nrb}	+0.3	Yes	No
R_{nrbc}	+0.3	Yes	Yes
R_{sr}	−3.0 (Box_L) −3.0 (Box_H) +0.3 (Box_D)	No	No
R_{srb}	same as R_{sr}	Yes	No
R_{srbc}	same as R_{sr}	Yes	Yes

Note. Considered fractionation processes are shown in columns under "$Fract_{bio}$" and "$Fract_{compl}$".

A constant ligand concentration of 1 μmol m^{-3} is used in the standard experiments, while a set of sensitivity experiments were performed with ligand concentration ranging from typical deep-ocean ligand concentrations of 0.6 and 1 μmol m^{-3} which are commonly assumed in global iron models, to higher values of 1.5 and 2.0 μmol m^{-3} which are still within the range of measured ligand concentrations (Gledhill & Buck, 2012). Details of these experiments are shown in Figure S8 in Supporting Information S1.

2.3. Model Experiments

Due to very different isotopic end-member signatures between the reductive and non-reductive sediment source, and the high uncertainty in the strength of the sedimentary iron into the ocean, nine sets of sensitivity simulations with differing isotopic end-member signature of the sedimentary iron were conducted in this study: three with a reductive sediment source (experiment names containing "r"), three with a non-reductive source (experiment names containing "nr") and three with a reductive source for the surface ocean boxes Box_L and Box_H and a non-reductive source for the deep ocean box Box_D (experiment names containing "sr") (Table 3).

For each assumption on the isotopic end-member signature of the sediment source, we performed three substudies: one without any fractionation effects in the water column, one with biological fractionation (experiment names containing "b"), and one with fractionation during biological uptake and through organic complexation (experiment names containing "bc"). In each of these nine experiment groups we then varied the strength of the sedimentary source by multiplying it with a factor ranging from 1 to 200 in 8 steps, leaving the strength of the other Fe sources constant. As the strengthening of the sediment source would otherwise lead to overly large DFe concentrations, we also varied the scavenging rate to keep DFe concentrations in each box close to observations (also see Section 2.4). The detailed factors are given in Table 4.

Existing measurements of iron isotopic composition in marine sediments show that, while reductive sedimentary sources are often found where organic carbon supply is high, for example, in marginal shelves and under productive upwelling regions (Fitzsimmons & Conway, 2023; Henkel et al., 2018; Homoky et al., 2009; Severmann et al., 2006, 2010), non-reductive signals are rather reported in oxic sediment pore waters which may dominate in deeper parts of the ocean (Fitzsimmons & Conway, 2023; Homoky et al., 2009, 2011, 2013; Labatut et al., 2014). Exceptions are found in shallower waters with low biological productivity and in the Oxygen Minimum Zones (OMZs) with intermediate water depths. Low biological productivity leads to less oxygen consumption by oxic degradation of organic matter and thus, sediments could be a non-reductive input of iron (Labatut et al., 2014). Some OMZs are distributed from the mesopelagic to a part of the bathypelagic zone. Sedimentary iron there keeps its reductive signals also in deep waters (Staubwasser et al., 2006). Therefore, in the last three sets of experiments, we assume a non-reductive sedimentary source for Box_D and a reductive source for the two surface boxes. Results from a previous modeling study by König et al. (2021) also show that sediments generally supply isotopically light Fe into the upper ocean but heavier ones deeper in the water column. During the model-data comparison (Section 2.4), we were aware that deeper OMZs are included in the eastern part of GEOTRACES cruise GP16 in the tropical Pacific Ocean, although the observed seawater δ^{56}Fe in the deep ocean is dominated by open ocean samples. Our assumption of a non-reductive sedimentary input into Box_D can therefore not represent iron sources from those deeper OMZs. Yet, observations in the eastern part of GP16 were not excluded in the model-data

Table 4
Factors by Which the Strength of the Sedimentary Iron Source Was Multiplied in the Sensitivity Experiments, and the Corresponding Scavenging Rate in the Upper Model Boxes

Abbreviation	1X	2X	5X	10X	20X	50X	100X	200X
Sediment factor	1	2	5	10	20	50	100	200
Scavenging rate (day^{-1})	0.055	0.073	0.12	0.195	0.34	0.8	1.6	3.2

Note. Scavenging rate in the lower box was always 1% of that in the upper boxes.

comparison, since we rather compared with the median of data sorted to the deep-ocean box which may not be strongly affected by the small number of lighter isotopic compositions along GP16 (Figure S2 in Supporting Information S1).

Each experiment was run for 10,000 years to ensure that DFe and ^{56}Fe reach their equilibrium concentrations.

2.4. Model-Data Comparison

For model validation, measured concentrations of DFe and iron isotopic composition δ^{56}Fe were taken from GEOTRACES, 2021 and other previous studies by Conway and John (2015); Fitzsimmons et al. (2015); John and Adkins (2012); Kurisu et al. (2024); Labatut et al. (2014); Lacan et al. (2008); Radic et al. (2011); Sieber et al. (2021); Zhang et al. (2021) (Figure S1 in Supporting Information S1, Table S3). The lowest values are found in the high-latitude North Pacific, close to coasts where the reductive sedimentary source probably dominates, and in the deep North Atlantic close to the Mid-Atlantic Ridge (Conway & John, 2014), while the highest values were measured in the surface Southern Ocean around the Antarctica and in the eastern equatorial Pacific which might be strongly influenced by local iron sources such as meltwater (Sieber et al., 2021) and dust deposition (John et al., 2018). All data are sorted into the three model boxes, defined by latitude, longitude and water depth, according to the expansion of the model boxes (Section 2.1). Median, 10th and 90th percentile of δ^{56}Fe were calculated for each box and plotted along the entire range of observations in Figure 5.

For each magnitude of the sedimentary iron source prescribed in the model, 11 tuning runs were conducted varying the scavenging rate. The criterion to determine the "best" source strength-scavenging rate pair is that the modeled DFe concentration in each box is between the 40th and 60th percentile of the measurements. If more than one tuning run fulfills this criterion, the one whose DFe concentrations are closer to the median of observations was chosen. The 40th and 60th percentile, and the median of observed DFe sorted to Box$_L$ are 0.16, 0.26, and 0.20 μmol m^{-3}; to Box$_H$: 0.24, 0.46, and 0.34 μmol m^{-3}; and to Box$_D$ are 0.51, 0.65, and 0.57 μmol m^{-3}, respectively. The outcome of that exercise is documented in the lower row in Table 4.

3. Results and Discussion

3.1. Role of the Sediment Isotopic Composition

We first analyze the effects of reductive versus non-reductive sedimentary sources in the set of experiments without fractionation in the water column, so that the differences between the experiments can only be explained by the different end-member signatures of the sedimentary source. Figure 2 compares how δ^{56}Fe evolves in the three ocean boxes with changing total sedimentary source in the experiments R$_r$, R$_{nr}$ and R$_{sr}$, assuming different isotopic compositions of the sedimentary source end-member (Table 3).

Assuming the sedimentary source to be purely reductive (R$_r$, the solid line with "×" in the three subfigures), the values of δ^{56}Fe are very similar in all three boxes, and change from a mixture of the isotopic signals between sedimentary and dust source, for low sedimentary source strength, to a uniform ocean representing only the end-member signature of the sediment at high sedimentary source. Only Box$_L$ (in the left subfigure) shows slightly heavier δ^{56}Fe values with low to medium sedimentary sources (1–5 fold source enhancement). There, the dust source with a much heavier isotopic composition contributes at a higher or comparable rate to the sedimentary source, whereas no dust source is considered in Box$_H$ and Box$_D$.

Although the values of δ^{56}Fe are much higher than in R$_r$, the qualitative picture is similar (R$_{nr}$, the solid line with "○" in the three subfigures, assuming a purely non-reductive sediment iron source): the three ocean boxes show almost uniform values of δ^{56}Fe which evolve from a mixture of the isotopic signals of the dust and sediment source at low sedimentary iron fluxes, to a pure reflection of the sedimentary source at high sedimentary input.

It is only when assuming a mixture of reductive and non-reductive sedimentary sources (R$_{sr}$, the solid line with "△" in the three subfigures) that we find significant differences in the isotopic values of the three boxes. The sedimentary input into Box$_D$ is assumed to be non-reductive, thus δ^{56}Fe in Box$_D$ are the highest, close to the values in R$_{nr}$. Box$_L$ and Box$_H$ shows a declining trend with the source strength, explained by the increasing contribution of reductive sediments in these two boxes. Values in Box$_H$ are higher than in Box$_L$, mainly driven by the mixing between Box$_H$ with reductive sediments and Box$_D$ with non-reductive sediments.

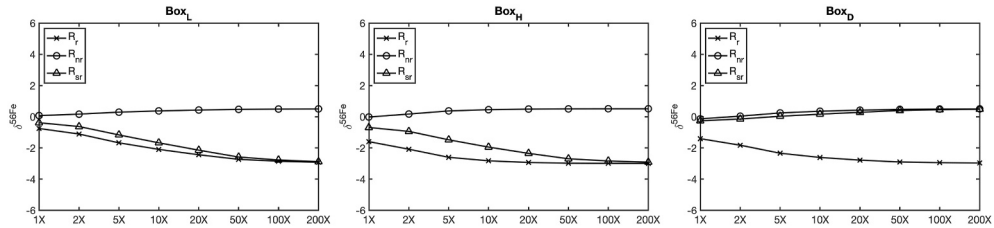

Figure 2. δ^{56}Fe in the low-latitude surface box Box_L, high-latitude surface box Box_H and deep-ocean box Box_D in the experiments R_r, R_{nr} and R_{sr} (see experiment names in Table 3). The *X*-axis shows the enhancement factor of the sedimentary source.

3.2. Role of Biological Fractionation: R_{nr} versus R_{nrb}, and R_{sr} versus R_{srb}

How fractionation by biological uptake affects δ^{56}Fe can be easily seen when comparing R_{nr} and R_{nrb} (Figure 3a, lines with "o" and those with "×"), since all three boxes in R_{nr} have near-zero values, serving best as a reference. Biological fractionation creates large inter-box variability with $Box_L > Box_H > Box_D$. Lighter isotopes are preferentially taken up by phytoplankton in surface boxes and thus more heavier isotopes are left in seawater, resulting in a higher δ^{56}Fe. In the deep ocean box organic matter is remineralized, releasing more lighter isotopes and decreasing δ^{56}Fe in Box_D. Values in Box_H lie between Box_L and Box_D, affected by the mixing between Box_H and Box_D. The large inter-box variability converges with increasing sedimentary source until the effect of biological fractionation is negligibly small compared to that of the sedimentary input. Thus, δ^{56}Fe in all three boxes become closer to those in R_{nr} without biological fractionation.

Patterns in R_{sr} and R_{srb} look more complex (Figure 3b). Ignoring biological fractionation (R_{sr}), δ^{56}Fe in the three boxes diverge from the initial near-zero values with the increasing source strength; while biological fractionation creates large inter-box differences in sensitivity simulations with lower sedimentary sources which decrease with increasing source strength, similar to the effect of biological fractionation in R_{nrb}. With higher sedimentary sources, values in all ocean boxes are getting closer to those in R_{sr}. Therefore, the different patterns in Figures 3a and 3b are mainly driven by the different isotopic composition of sediments in different ocean boxes.

3.3. Role of Fractionation by Organic Complexation: R_{nrb} versus R_{nrbc}, and R_{srb} versus R_{srbc}

Assuming non-reductive sediments in all three boxes and considering biological fractionation (R_{nrb}), δ^{56}Fe starts with positive values in Box_L and negative values in Box_H and Box_D when sedimentary sources are low, and converges to values slightly above +1‰with increasing source strength. These features have been already discussed in the last chapter (Section 3.2, Figure 3). Comparing R_{nrb} (Figure 4a, lines with "o") with R_{nrbc} (Figure 4a, lines with "×"), one can easily see that the fractionation by organic complexation shifts δ^{56}Fe completely into the positive range and the magnitude of the shifts is larger at lower source strengths (up to 6‰) and reduces to around 2‰ at a 200-fold enhancement of the sedimentary source.

Heavier iron isotopes are preferentially bound in organic complexes, resulting in a higher scavenging loss of lighter isotopes. This fractionation process moves isotopic compositions throughout the water column into positive direction, not like biological uptake which acts in the surface and deep open in opposite directions. Thus, with strong sedimentary sources, even though the non-reductive source signal dominates in all ocean boxes, the converged δ^{56}Fe values in R_{nrbc} are higher than those in R_{nrb}. Furthermore, the fractionation through organic complexation reduces the inter-box variability in simulations with lower sedimentary sources: for example, in the simulation with the initial source strength, δ^{56}Fe in the three boxes span over 7‰ in R_{nrb}, while in R_{nrbc} they vary from +0.9‰ to +4.8‰. The scavenging of free iron ions in our model is highest in Box_H (Table S2) due to the highest iron concentrations and the applied higher scavenging rate for surface boxes (Table 2), representing the higher particle load and reactivity there. Therefore, δ^{56}Fe in Box_H is most fractionated through organic complexation or rather scavenging (Table S2) which strongly influences δ^{56}Fe in Box_D by mixing. With the convergence of three ocean boxes with the increasing source strength, differences in the inter-box variability between R_{nrb} and R_{nrbc} also vanish.

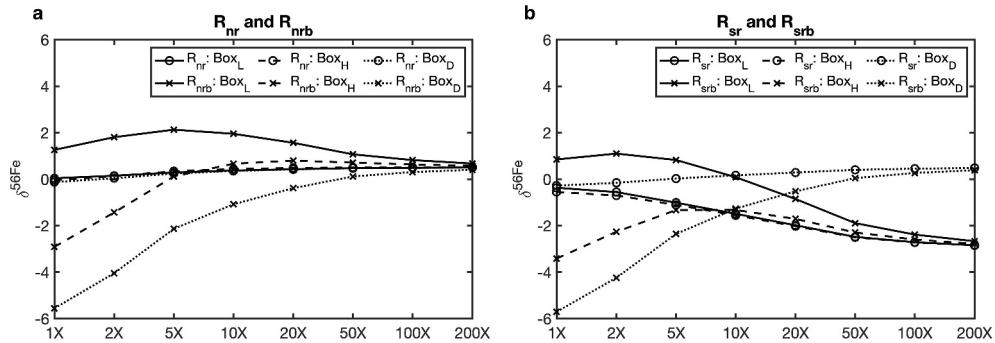

Figure 3. Comparison of δ^{56}Fe in the low-latitude surface box Box_L, high-latitude surface box Box_H and deep-ocean box Box_D in the experiments: (a) R_{nr} and R_{nrb}, (b) R_{sr} and R_{srb}, to illustrate the role of biological fractionation in changing the seawater iron isotopic composition. The *X*-axis shows the enhancement factor of the sedimentary source.

Considering different end-member signatures of the sedimentary source introduces a bit higher complexity in the comparison of R_{srb} and R_{srbc} (Figure 4b). However, comparing Figure 4b with Figure 3b, one reveals that the "X"-form evolution between the surface boxes and the deep one is already featured by biological fractionation. The fractionation through organic complexation just introduces an offset between R_{srb} and R_{srbc} in each ocean box which remains in all simulations. The reason for the offsets has been mentioned in the last paragraph.

3.4. Constraints on the Sedimentary Iron Source

One of the key questions in the research field of marine iron isotopes is whether we can better constrain strengths of external iron sources into the ocean based on measured isotopic compositions and understanding of fractionation processes. To this end, model results of the three experiments considering both fractionation through biological uptake and organic complexation but different end-member signatures of the sedimentary source (R_{rbc}, R_{nrbc} and R_{srbc} in Figure 5) have been compared with ranges and median values of measured iron isotope concentrations (Section 2.4).

Assuming a reductive sediments source, δ^{56}Fe in R_{rbc} vary within the total ranges of observations when the sediment source is enhanced by 50 times and above. However, all three ocean boxes show only negative δ^{56}Fe values and Box_D always has lower values than Box_H, disagreeing with the observed medians.

Non-reductive sediments (R_{nrbc}) shift δ^{56}Fe in all boxes into the positive range. With smaller sedimentary sources, δ^{56}Fe in Box_D is within the range of observations, while the surface boxes show too heavy isotopic compositions. All the values become closer to about 3‰ with increasing sedimentary input and with 200 times enhanced sediments they are still beyond the observed ranges. This indicates that extremely high sedimentary sources are necessary to force δ^{56}Fe to the observed lower values. With that, however, the inter-box variability would vanish completely.

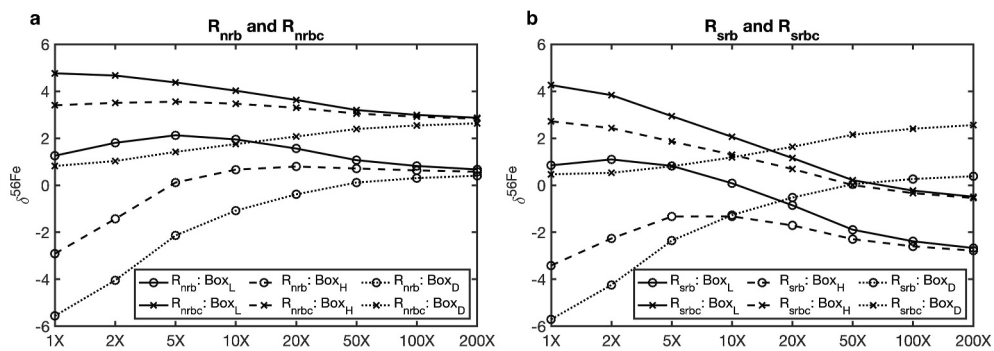

Figure 4. Comparison of δ^{56}Fe in the low-latitude surface box Box_L, high-latitude surface box Box_H and deep-ocean box Box_D in the experiments: (a) R_{nrb} and R_{nrbc}, (b) R_{srb} and R_{srbc}, to illustrate the role of fractionation by organic complexation in changing the seawater iron isotopic composition. The *X*-axis shows the enhancement factor of the sedimentary source.

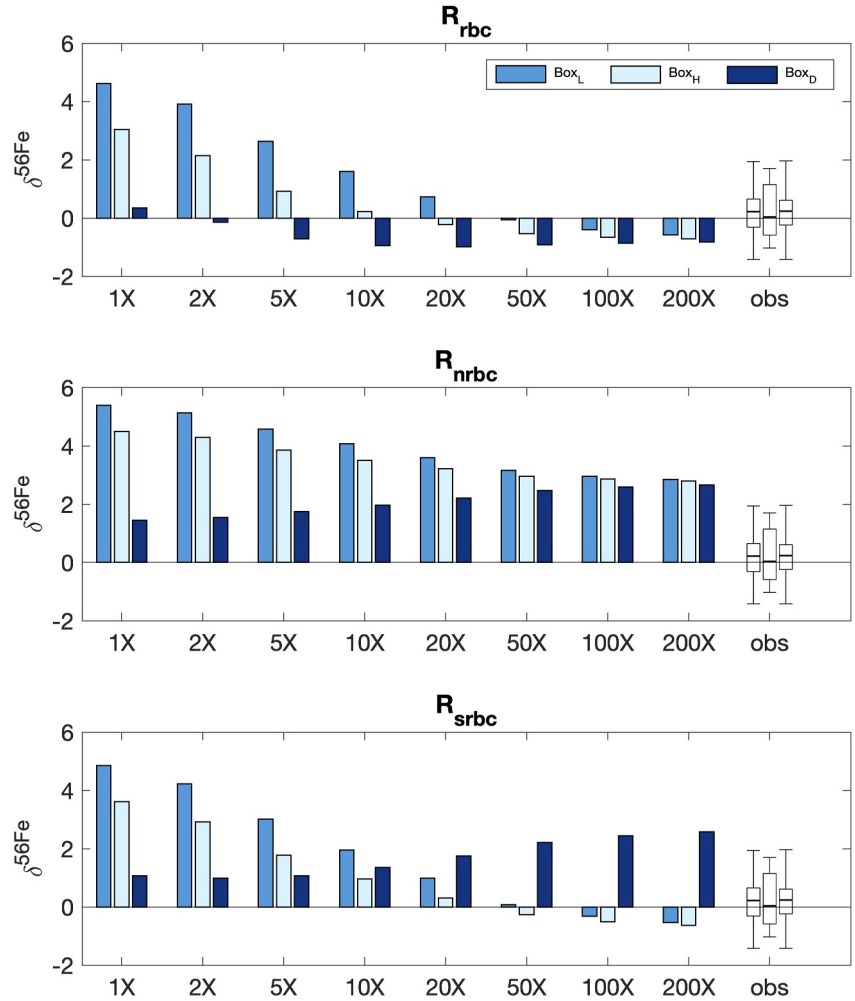

Figure 5. Comparison of δ^{56}Fe (‰) in three sets of simulations considering a reductive sedimentary source (R_{rbc}), a non-reductive sedimentary source (R_{nrbc}) and both reductive and non-reductive sedimentary source (R_{srbc}) with measurements ("obs") as white boxes. The *X*-axis shows the enhancement factor of the sedimentary source from 1 to 200. Observations were sorted into the three model boxes (Section 2.4). The 10th and 90th percentile of each model box are shown as vertical bars and the total range as whiskers. The median values are marked by the horizontal line within the bars.

In simulations of R_{srbc} with the medium-size sedimentary input (from 10-fold to 20-fold, corresponding to 7.5–15 Gmol yr^{-1}), the model achieved a pattern with all values within the observed ranges and lower values in Box_H than in the other two boxes. The latter can be only explained by the combined effect of different end-member signatures of the sedimentary source, mixing between Box_H and Box_D and fractionation processes. The end-member signature of the sedimentary source to Box_H is strongly negative, as one can clearly see in R_{sr}. Biological uptakes works against the negative source signal and drives δ^{56}Fe in both surface boxes to the positive ranges, while remineralization releases lighter iron isotopes in Box_D, which has already been discussed in Section 3.2. The high-latitude mixing brings isotopically lighter waters from Box_D to Box_H which lowers δ^{56}Fe in Box_H comparing to Box_L. Different to R_{srb}, scavenging preferentially removes iron with lighter isotopic compositions and acts against the negative trend in Box_D. This inter-box variability can only be retained as long as it is predominantly determined by fractionation processes, not by the end-member signatures of the sedimentary source. Therefore, the best model-data match is found in a relatively narrow range of the source strength.

This range of sedimentary iron input is constrained under the assumption of fixed end-member signatures of dust and hydrothermal source and their source strengths. Additional sets of experiments (Table S1 in Supporting Information S1) with a fixed end-member signature of sedimentary source but varying signatures of the other two sources show that our estimation of the strength of sedimentary iron input is rather robust against the variability in

end-member signals of dust and hydrothermal source (Figure S3 and Figure S4 in Supporting Information S1). The constrained sedimentary source is yet sensitive to the end-member signal of the sedimentary source (Figure S5 and Figure S6 in Supporting Information S1). Assuming less heavier non-reductive sedimentary source (+0.0‰ and +0.1‰) to the deep-ocean box results in a wider range of constrained sedimentary input between 7.5 and 37.5 Gmol yr^{-1}; while assuming a less negative isotopic composition for the reductive sediment input to the surface oceans (−2.4‰ and −1.8‰), δ^{56}Fe values remain within the observed range only in simulations with 20-fold sedimentary input or 15 Gmol yr^{-1} and those with smaller sedimentary input have too high δ^{56}Fe in Box_L. This high sensitivity suggests that further constraining should be done in studies considering the spatial variability in the end-member signature of the sedimentary iron input and in strengths of different iron sources as well as mechanisms determining these variabilities.

The constrained range of the sedimentary input remains unchanged among all experiments with different ligand concentrations, except for the experiment with the lowest ligand concentration (0.6 μmol m^{-3}) (Figure S7 in Supporting Information S1). In that experiment, a relatively low scavenging rate is required due to the low binding capacity of ligand, which failed to keep DFe concentration in Box_H within the observed range when the sedimentary input is increased by over 5 times.

4. Conclusions

Each of the nine sets of experiments, differing in the chosen isotopic signal of the sediment and the absence or presence of the two fractionation processes considered, demonstrates a clear dependency of seawater δ^{56}Fe on the strength of the sedimentary source and the corresponding scavenging rate. A convergence of the isotopic signal to a sediment-dominated value is found in all experiments with high source strengths. Generally, source strengths and end-member signatures create the framework for seawater δ^{56}Fe and fractionation and loss processes intensify spatial gradients which are important to be compatible with observed distributions of isotopic composition.

Assuming that the experiment sets that take into account both fractionation through biological uptake and organic complexation can best represent processes driving the cycle of iron isotopes in the real world (consistent with the findings in König et al., 2021; König et al., 2022), our results indicate that spatially variable end-member signatures of the sedimentary source are necessary to reproduce the observed range and inter-box variability of δ^{56}Fe, particularly for the high-latitude surface regions that are strongly influenced by mixing with the deep ocean and the biological fractionation taking place in the low-latitude surface ocean.

In comparison with observed seawater isotopic compositions, the best model-data match has been found in those simulations of R_{srbc} that have a 10- to 20-fold increase of the sedimentary source relative to our reference simulation. This suggests a global sedimentary input of DFe between 7.5 and 15 Gmol yr^{-1} and scavenging rates of 0.20–0.34 day^{-1} in surface waters, resulting in a residence time of 1–2 years. The numbers for sedimentary input are within the range of assumptions made in global models (<1–200 Gmol yr^{-1}) but lower than that many models assumed (around 100 Gmol yr^{-1}) (Somes et al., 2021; Tagliabue et al., 2016). The residence time in surface waters is within the range of measurement-based estimates from months to a few years (Black et al., 2020).

Since this simple box model only takes into account three ocean boxes, it obviously cannot reproduce isotopic gradients within individual ocean basins that have been the focus of many observational (e.g., Conway & John, 2014; Conway & John, 2015) and modeling (König et al., 2022) studies. Both due to the spatial simplification and the additional simplifications involved, namely the consideration of only three external iron sources, and simplifications in the representation of biological processes that are necessary in box models (e.g., a complete consumption of nutrients in Box_L), the modeled cycling of iron and its isotopes differs from that in more complex global biogeochemistry models and observations. A further limitation of our approach is that all scavenging is assumed to be irreversible. Reversible scavenging has been shown to transport isotopic signals from the surface downward for lead and zinc (Lanning et al., 2023; Sieber et al., 2023), and is likely to do the same for iron. A description of reversible scavenging, however, requires a description of vertical particle distributions (Roshan et al., 2020; Weber et al., 2018), which would introduce a number of additional assumptions into our model. Therefore, the optimized range of the sedimentary sources and scavenging rates resulted in this study needs to be further explored in full ocean biogeochemical models which also contain some description of particle (both biotic and abiotic) cycling.

Moreover, the assumption made of a uniform isotope signal of the sediment source signals within the different ocean boxes is strongly simplified and ignores spatial gradients caused for example, by productivity gradients, that, however, cannot be represented in a box model. A more realistic description based on processes regulating the source signals (e.g., the bottom water oxygen concentrations and sedimentary redox processes, such as represented in Dale et al. (2015)) is desirable in complex global models and might lead to optimal pairs of the sedimentary source strength and scavenging rate that are different from the ones obtained here. Nevertheless, the procedure established in this study (based on model-data comparison of iron isotopes) can be used to optimize or constrain the pair of the sedimentary source and scavenging rate in global iron models, helping to reduce uncertainties in assumed source strengths (Tagliabue et al., 2016). With this, an inter-model comparison could focus more on inneroceanic processes affecting the iron cycle in models, and reduce the strong dependency of model outcomes on difference in assumption on the strength of iron sources between models.

Appendix A: Calculation of δ^{56}Fe from Box Model Results

In the model, we have concentrations of Fe and ^{56}Fe. From these values we want to calculate δ^{56}Fe. The problem is that this quantity is related to the ratio of the two isotopes $r^{56} = {}^{56}\mathrm{Fe}/{}^{54}\mathrm{Fe}$, and not to the ratio $R^{56} = {}^{56}\mathrm{Fe}/\mathrm{Fe}_T$, where $\mathrm{Fe}_T = {}^{54}\mathrm{Fe} + {}^{56}\mathrm{Fe} + {}^{57}\mathrm{Fe} + {}^{58}\mathrm{Fe}$ is the sum of the concentrations of all stable Fe isotopes.

To get from R^{56} to r^{56} we use first the definition of Fe_T through

$$\begin{aligned}\mathrm{Fe}_T &= {}^{54}\mathrm{Fe} + {}^{56}\mathrm{Fe} + {}^{57}\mathrm{Fe} + {}^{58}\mathrm{Fe} \\ &= {}^{54}\mathrm{Fe}\cdot\left(1 + r^{56} + r^{57} + r^{58}\right) \\ &= {}^{54}\mathrm{Fe}\cdot\left(1 + \left(1+\delta^{56}\mathrm{Fe}\right)\cdot r^{56}_{\mathrm{std}} + \left(1+\delta^{57}\mathrm{Fe}\right)\cdot r^{57}_{\mathrm{std}} + \left(1+\delta^{58}\mathrm{Fe}\right)\cdot r^{58}_{\mathrm{std}}\right)\end{aligned} \tag{A1}$$

where $\alpha^n = 1 + \delta^n\mathrm{Fe} = r^r/r^n_{\mathrm{std}}$ is the isotopic ratio of a sample (for an isotope with atomic weight n) divided by the isotopic ratio of the standard.

In the next step we use the fact that isotopic fractionation for iron isotopes is usually mass dependent, so $\delta^{57}\mathrm{Fe} = 3/2\cdot\delta^{56}\mathrm{Fe}$ and $\delta^{58}\mathrm{Fe} = 2\delta^{56}\mathrm{Fe}$, to obtain

$$\mathrm{Fe}_T = {}^{54}\mathrm{Fe}\cdot\left(1 + r^{56}_{\mathrm{std}} + r^{57}_{\mathrm{std}} + r^{58}_{\mathrm{std}} + \delta^{56}\mathrm{Fe}\cdot\left(r^{56}_{\mathrm{std}} + \frac{3}{2}r^{57}_{\mathrm{std}} + 2r^{58}_{\mathrm{std}}\right)\right) \tag{A2}$$

an equation that now only contains the two unknowns ^{54}Fe and δ^{56}Fe.

The required second equation comes from combining the two definitions of isotopic ratios R^{56} and r^{56}: We have

$$\begin{aligned}{}^{56}\mathrm{Fe} &= \mathrm{Fe}_T\cdot R^{56} \\ &= {}^{54}\mathrm{Fe}\cdot r^{56} = {}^{54}\mathrm{Fe}\cdot\left(1+\delta^{56}\mathrm{Fe}\right)\cdot r^{56}_{\mathrm{std}}\end{aligned} \tag{A3}$$

which we can use to write $\mathrm{Fe}_T = {}^{54}\mathrm{Fe}\cdot\left(1+\delta^{56}\mathrm{Fe}\right)\cdot r^{56}_{\mathrm{std}}/R^{56}$. Inserting this into Equation A2 and canceling out the concentration of ^{54}Fe we obtain a single equation for δ^{56}Fe:

$$\left(1+\delta^{56}\mathrm{Fe}\right)r^{56}_{\mathrm{std}} = R^{56}\cdot\left(1 + r^{56}_{\mathrm{std}} + r^{57}_{\mathrm{std}} + r^{58}_{\mathrm{std}} + \delta^{56}\mathrm{Fe}\cdot\left(r^{56}_{\mathrm{std}} + \frac{3}{2}r^{57}_{\mathrm{std}} + 2r^{58}_{\mathrm{std}}\right)\right), \tag{A4}$$

and the solution to this is

$$\delta^{56}\mathrm{Fe} = \frac{R^{56}\cdot\left(1 + r^{56}_{\mathrm{std}} + r^{57}_{\mathrm{std}} + r^{58}_{\mathrm{std}}\right) - r^{56}_{\mathrm{std}}}{r^{56}_{\mathrm{std}} - R^{56}\cdot\left(r^{56}_{\mathrm{std}} + 3r^{57}_{\mathrm{std}}/2 + 2r^{58}_{\mathrm{std}}\right)} \tag{A5}$$

Data Availability Statement

The source code of the box model used for this manuscript is archived on Zenodo (Ye, 2025a). Model output (Table S2) and additional observational data collected from publications (Table S3) are also available on Zenodo (Ye, 2025b).

Acknowledgments
This work was supported by the German Research Foundation (DFG) project (Grant YE 170/2-1). Open Access funding enabled and organized by Projekt DEAL.

References

Abadie, C., Lacan, F., Radic, A., Pradoux, C., & Poitrasson, F. (2017). Iron isotopes reveal distinct dissolved iron sources and pathways in the intermediate versus deep Southern Ocean. *Proceedings of the National Academy of Sciences*, *114*(5), 858–863. https://doi.org/10.1073/pnas.1603107114

Beard, B. L., & Johnson, C. M. (2004). Fe Isotope variations in the modern and Ancient Earth and other planetary bodies. *Reviews in Mineralogy and Geochemistry*, *55*(1), 319–357. https://doi.org/10.2138/gsrmg.55.1.319

Beard, B. L., Johnson, C. M., Von Damm, K. L., & Poulson, R. L. (2003). Iron isotope constraints on Fe cycling and mass balance in oxygenated Earth oceans. *Geology*, *31*(7), 629–632. https://doi.org/10.1130/0091-7613(2003)031⟨0629:IICOFC⟩2.0.CO;2

Bennett, S. A., Rouxel, O., Schmidt, K., Garbe-Schönberg, D., Statham, P. J., & German, C. R. (2009). Iron isotope fractionation in a buoyant hydrothermal plume, 5 S Mid-Atlantic Ridge. *Geochimica et Cosmochimica Acta*, *73*(19), 5619–5634. https://doi.org/10.1016/j.gca.2009.06.027

Bergquist, B. A., & Boyle, E. A. (2006). Iron isotopes in the Amazon River system: Weathering and transport signatures. *Earth and Planetary Science Letters*, *248*(1–2), 54–68. https://doi.org/10.1016/j.epsl.2006.05.004

Black, E., Kienast, S. S., Lemaitre, N., Lam, P. J., Anderson, R. F., Planquette, H., et al. (2020). Ironing out fe residence time in the dynamic upper ocean. *Global Biogeochemical Cycles*, *34*(9), e2020GB006592. https://doi.org/10.1029/2020gb006592

Chen, T., Li, W., Guo, B., Liu, R., Li, G., Zhao, L., & Ji, J. (2020). Reactive iron isotope signatures of the east asian dust particles: Implications for iron cycling in the deep north pacific. *Chemical Geology*, *531*, 119342. https://doi.org/10.1016/j.chemgeo.2019.119342

Conway, T. M., & John, S. G. (2014). Quantification of dissolved iron sources to the North Atlantic ocean. *Nature*, *511*(7508), 212–215. https://doi.org/10.1038/nature13482

Conway, T. M., & John, S. G. (2015). The cycling of iron, zinc and cadmium in the North East Pacific Ocean – Insights from stable isotopes. *Geochimica et Cosmochimica Acta*, *164*, 262–283. https://doi.org/10.1016/j.gca.2015.05.023

Crosby, H. A., Johnson, C. M., Roden, E. E., & Beard, B. L. (2005). Coupled Fe(II)-Fe(III) electron and atom exchange as a mechanism for Fe isotope fractionation during dissimilatory iron oxide reduction. *Environmental Science and Technology*, *39*(17), 6698–6704. https://doi.org/10.1021/es0505346

Crosby, H. A., Roden, E. E., Johnson, C. M., & Beard, B. L. (2007). The mechanisms of iron isotope fractionation produced during dissimilatory Fe(III) reduction by Shewanella putrefaciens and Geobacter sulfurreducens. *Geobiology*, *5*(2), 169–189. https://doi.org/10.1111/j.1472-4669.2007.00103.x

Dale, A. W., Nickelsen, L., Scholz, F., Hensen, C., Oschlies, A., & Wallmann, K. (2015). A revised global estimate of dissolved iron fluxes from marine sediments. *Global Biogeochemical Cycles*, *29*(5), 691–707. https://doi.org/10.1002/2014GB005017

Dauphas, N., John, S. G., & Rouxel, O. (2017). Iron isotope systematics. *Reviews in Mineralogy and Geochemistry*, *82*(1), 415–510. https://doi.org/10.2138/rmg.2017.82.11

de Baar, H. J. W., & de Jong, J. (2001). Distributions, sources and sinks of iron in seawater. In D. R. Turner & K. A. Hunter (Eds.), *The biogeochemistry of iron in seawater* (Vol. 7, pp. 123–253). John Wiley and Sons.

Dideriksen, K., Baker, J. A., & Stipp, S. L. S. (2008). Equilibrium Fe isotope fractionation between inorganic aqueous Fe(III) and the siderophore complex, Fe(III)-desferrioxamine B. *Earth and Planetary Science Letters*, *269*(1), 280–290. https://doi.org/10.1016/j.epsl.2008.02.022

Duce, R. A., & Tindale, N. W. (1991). Atmospheric transport of iron and its deposition in the ocean. *Limnology & Oceanography*, *36*(8), 1715–1726. https://doi.org/10.4319/lo.1991.36.8.1715

Elderfield, H., & Schultz, A. (1996). Mid-ocean ridge hydrothermal fluxes and the chemical composition of the ocean. *Annual Review of Earth and Planetary Sciences*, *24*(1), 191–224. https://doi.org/10.1146/annurev.earth.24.1.191

Ellwood, M. J., Hutchins, D. A., Lohan, M. C., Milne, A., Nasemann, P., Nodder, S. D., et al. (2015). Iron stable isotopes track pelagic iron cycling during a subtropical phytoplankton bloom. *PNAS*, *112*(1), E15–E20. https://doi.org/10.1073/pnas.1421576112

Ellwood, M. J., Strzepek, R. F., Strutton, P. G., Trull, T. W., Fourquez, M., & Boyd, P. W. (2020). Distinct iron cycling in a southern ocean eddy. *Nature Communications*, *11*(1), 825. https://doi.org/10.1038/s41467-020-14464-0

Elrod, V. A., Berelson, W. M., Coale, K. H., & Johnson, K. S. (2004). The flux of iron from continental shelf sediments: A missing source for global budgets. *Geophysical Research Letters*, *31*(12), L12307. https://doi.org/10.1029/2004GL020216

Escoube, R., Rouxel, O. J., Pokrovsky, O. S., Schroth, A., Max Holmes, R., & Donard, O. F. (2015). Iron isotope systematics in Arctic rivers. *Comptes Rendus Geoscience*, *347*(7–8), 377–385. https://doi.org/10.1016/j.crte.2015.04.005

Escoube, R., Rouxel, O. J., Sholkovitz, E., & Donard, O. F. (2009). Iron isotope systematics in estuaries: The case of North River, Massachusetts (USA). *Geochimica et Cosmochimica Acta*, *73*(14), 4045–4059. https://doi.org/10.1016/j.gca.2009.04.026

Fitzsimmons, J. N., Carrasco, G. G., Wu, J., Roshan, S., Hatta, M., Measures, C. I., et al. (2015). Partitioning of dissolved iron and iron isotopes into soluble and colloidal phases along the GA03 GEOTRACES North Atlantic Transect. *Deep Sea Research Part II: Topical Studies in Oceanography*, *116*, 130–151. https://doi.org/10.1016/j.dsr2.2014.11.014

Fitzsimmons, J. N., & Conway, T. M. (2023). Novel insights into marine iron biogeochemistry from iron isotopes. *Annual Review of Marine Science*, *15*(1), 383–406. https://doi.org/10.1146/annurev-marine-032822-103431

Geotraces, I. D. P. (2021). Geotraces intermediate data product group (2021). https://doi.org/10.5285/cf2d9ba9-d51d-3b7c-e053-8486abc0f5fd

Gerringa, L. J. A., Alderkamp, A.-C., Laan, P., Thuroczy, C.-E., De Baar, H. J. W., Mills, M. M., et al. (2012). Iron from melting glaciers fuels the phytoplankton blooms in amundsen sea (southern ocean): Iron biogeochemistry. *Deep Sea Research Part II: Topical Studies in Oceanography*, *71*, 16–31. https://doi.org/10.1016/j.dsr2.2012.03.007

Gledhill, M., & Buck, K. N. (2012). The organic complexation of iron in the marine environment: A review. *Frontiers in Microbiology*, *3*, 1–17. https://doi.org/10.3389/fmicb.2012.00069

Guieu, C., Bonnet, S., Wagener, T., & Loÿe-Pilot, M.-D. (2005). Biomass burning as a source of dissolved iron to the open ocean? *Geophysical Research Letters*, *32*(19), L19608. https://doi.org/10.1029/2005gl022962

Hamilton, D. S., Moore, J. K., Arneth, A., Bond, T. C., Carslaw, K. S., Hantson, S., et al. (2020). Impact of changes to the atmospheric soluble iron deposition flux on ocean biogeochemical cycles in the Anthropocene. *Global Biogeochemical Cycles*, *34*(3), e2019GB006448. https://doi.org/10.1029/2019GB006448

Hamme, R. C., Webley, P. W., Crawford, W. R., Whitney, F. A., DeGrandpre, M. D., Emerson, S. R., et al. (2010). Volcanic ash fuels anomalous plankton bloom in subarctic northeast pacific. *Geophysical Research Letters*, *37*(19), L19604. https://doi.org/10.1029/2010GL044629

Henkel, S., Kasten, S., Hartmann, J. F., Silva-Busso, A., & Staubwasser, M. (2018). Iron cycling and stable fe isotope fractionation in antarctic shelf sediments, king george island. *Geochimica et Cosmochimica Acta*, *237*, 320–338. https://doi.org/10.1016/j.gca.2018.06.042

Henkel, S., Kasten, S., Poulton, S. W., & Staubwasser, M. (2016). Determination of the stable iron isotopic composition of sequentially leached iron phases in marine sediments. *Chemical Geology*, *421*, 93–102. https://doi.org/10.1016/j.chemgeo.2015.12.003

Homoky, W. B., Conway, T. M., John, S. G., König, D., Deng, F., Tagliabue, A., & Mills, R. A. (2021). Iron colloids dominate sedimentary supply to the ocean interior. *Proceedings of the National Academy of Sciences*, *118*(13), e2016078118. https://doi.org/10.1073/pnas.2016078118

Homoky, W. B., Hembury, D. J., Hepburn, L. E., Mills, R. A., Statham, P. J., Fones, G. R., & Palmer, M. R. (2011). Iron and manganese diagenesis in deep sea volcanogenic sediments and the origins of pore water colloids. *Geochimica et Cosmochimica Acta*, *75*(17), 5032–5048. https://doi.org/10.1016/j.gca.2011.06.019

Homoky, W. B., John, S. G., Conway, T. M., & Mills, R. A. (2013). Distinct iron isotopic signatures and supply from marine sediment dissolution. *Nature Communications*, *4*(1), 2143. https://doi.org/10.1038/ncomms3143

Homoky, W. B., Severmann, S., Mills, R. A., Statham, P. J., & Fones, G. R. (2009). Pore-fluid Fe isotopes reflect the extent of benthic Fe redox recycling: Evidence from continental shelf and deep-sea sediments. *Geology*, *37*(8), 751–754. https://doi.org/10.1130/g25731a.1

Homoky, W. B., Weber, T., Berelson, W. M., Conway, T. M., Henderson, G. M., van Hulten, M., et al. (2016). Quantifying trace element and isotope fluxes at the ocean–sediment boundary: A review. *Philosophical Transactions of the Royal Society A*, *374*(2081), 20160246. https://doi.org/10.1098/rsta.2016.0246

Hunter, K. A., & Boyd, P. W. (2007). Iron-binding ligands and their role in the ocean biogeochemistry of iron. *Environmental Chemistry*, *4*(4), 221–232. https://doi.org/10.1071/en07012

Ito, A. (2013). Global modeling study of potentially bioavailable iron input from shipboard aerosol sources to the ocean. *Global Biogeochemical Cycles*, *27*(1), 1–10. https://doi.org/10.1029/2012GB004378

John, S. G., & Adkins, J. (2012). The vertical distribution of iron stable isotopes in the North Atlantic near Bermuda. *Global Biogeochemical Cycles*, *26*(2), 1–10. https://doi.org/10.1029/2011GB004043

John, S. G., Helgoe, J., Townsend, E., Weber, T., DeVries, T., Tagliabue, A., et al. (2018). Biogeochemical cycling of fe and fe stable isotopes in the eastern tropical south pacific. *Marine Chemistry*, *201*, 66–76. https://doi.org/10.1016/j.marchem.2017.06.003

John, S. G., Mendez, J., Moffett, J., & Adkins, J. (2012). The flux of iron and iron isotopes from San Pedro Basin sediments. *Geochimica et Cosmochimica Acta*, *93*, 14–29. https://doi.org/10.1016/j.gca.2012.06.003

King, A., Sañudo-Wilhelmy, S., Boyd, P., Twining, B., Wilhelm, S., Breene, C., et al. (2012). A comparison of biogenic iron quotas during a diatom spring bloom using multiple approaches. *Biogeosciences*, *9*(2), 667–687. https://doi.org/10.5194/bg-9-667-2012

Klar, J. K., Homoky, W. B., Statham, P. J., Birchill, A. J., Harris, E. L., Woodward, E. M. S., et al. (2017). Stability of dissolved and soluble fe (ii) in shelf sediment pore waters and release to an oxic water column. *Biogeochemistry*, *135*(1–2), 49–67. https://doi.org/10.1007/s10533-017-0309-x

Kohfeld, K. E., & Ridgwell, A. (2009). Glacial-interglacial variability in atmospheric CO_2. *Surface Ocean/Lower Atmosphere Processes, Geophysical Monograph Series*, *37*, 251–286. https://doi.org/10.1029/2008GM000845

König, D., Conway, T., Hamilton, D., & Tagliabue, A. (2022). Surface ocean biogeochemistry regulates the impact of anthropogenic aerosol fe deposition on the cycling of iron and iron isotopes in the north pacific. *Geophysical Research Letters*, *49*(13), e2022GL098016. https://doi.org/10.1029/2022gl098016

König, D., Conway, T. M., Ellwood, M., Homoky, W., & Tagliabue, A. (2021). Constraints on the cycling of iron isotopes from a global ocean model. *Global Biogeochemical Cycles*, *35*(9), e2021GB006968. https://doi.org/10.1029/2021GB006968

Kurisu, M., Sakata, K., Nishioka, J., Obata, H., Conway, T. M., Hunt, H. R., et al. (2024). Source and fate of atmospheric iron supplied to the subarctic north pacific traced by stable iron isotope ratios. *Geochimica et Cosmochimica Acta*, *378*, 168–185. https://doi.org/10.1016/j.gca.2024.06.009

Labatut, M., Lacan, F., Pradoux, C., Chmeleff, J., Radic, A., Murray, J. W., et al. (2014). Iron sources and dissolved-particulate interactions in the seawater of the Western Equatorial Pacific, iron isotope perspectives. *Global Biogeochemical Cycles*, *28*(10), 1044–1065. https://doi.org/10.1002/2014GB004928

Lacan, F., Radic, A., Jeandel, C., Poitrasson, F., Sarthou, G., Pradoux, C., & Freydier, R. (2008). Measurement of the isotopic composition of dissolved iron in the open ocean. *Geophysical Research Letters*, *35*(24), 1–5. https://doi.org/10.1029/2008GL035841

Lanning, N. T., Jiang, S., Amaral, V. J., Mateos, K., Steffen, J. M., Lam, P. J., et al. (2023). Isotopes illustrate vertical transport of anthropogenic Pb by reversible scavenging within Pacific Ocean particle veils. *Proceedings of the National Academy of Sciences*, *120*(23), e2219688120. https://doi.org/10.1073/pnas.2219688120

Lannuzel, D., Schoemann, V., de Jong, J., Pasquer, B., van der Merwe, P., Masson, F., et al. (2010). Distribution of dissolved iron in antarctic sea ice: Spatial, seasonal, and inter-annual variability. *Journal of Geophysical Research*, *115*(G3), G03022. https://doi.org/10.1029/2009JG001031

Liu, X., & Millero, F. J. (2002). The solubility of iron in seawater. *Marine Chemistry*, *77*(1), 43–54. https://doi.org/10.1016/s0304-4203(01)00074-3

Martínez-García, A., Sigman, D. M., Ren, H., Anderson, R. F., Straub, M., Hodell, D. A., et al. (2014). Iron fertilization of the Subantarctic Ocean during the last ice age. *Science*, *343*(6177), 1347–1350. https://doi.org/10.1126/science.1246848

Mead, C., Herckes, P., Majestic, B. J., & Anbar, A. D. (2013). Source apportionment of aerosol iron in the marine environment using iron isotope analysis. *Geophysical Research Letters*, *40*(21), 5722–5727. https://doi.org/10.1002/2013GL057713

Morgan, J. L., Wasylenki, L. E., Nuester, J., & Anbar, A. D. (2010). Fe isotope fractionation during equilibration of Fe-organic complexes. *Environmental Science and Technology*, *44*(16), 6095–6101. https://doi.org/10.1021/es100906z

Nasemann, P., Gault-Ringold, M., Stirling, C. H., Koschinsky, A., & Sander, S. G. (2018). Processes affecting the isotopic composition of dissolved iron in hydrothermal plumes: A case study from the Vanuatu back-arc. *Chemical Geology*, *476*, 70–84. https://doi.org/10.1016/j.chemgeo.2017.11.005

Radic, A., Lacan, F., & Murray, J. W. (2011). Iron isotopes in the seawater of the equatorial Pacific Ocean: New constraints for the oceanic iron cycle. *Earth and Planetary Science Letters*, *306*(1–2), 1–10. https://doi.org/10.1016/j.epsl.2011.03.015

Raiswell, R. (2011). Iceberg-hosted nanoparticulate fe in the southern ocean: Mineralogy, origin, dissolution kinetics and source of bioavailable fe. *Deep Sea Research Part II: Topical Studies in Oceanography*, *58*(11–12), 1364–1375. https://doi.org/10.1016/j.dsr2.2010.11.011

Robinson, R. S., Brzezinski, M. A., Beucher, C. P., Horn, M. G., & Bedsole, P. (2014). The changing roles of iron and vertical mixing in regulating nitrogen and silicon cycling in the Southern Ocean over the last glacial cycle. *Paleoceanography*, *29*(12), 1179–1195. https://doi.org/10.1002/2014pa002686

Roshan, S., DeVries, T., Wu, J., John, S., & Weber, T. (2020). Reversible scavenging traps hydrothermal iron in the deep ocean. *Earth and Planetary Science Letters*, *542*, 116297. https://doi.org/10.1016/j.epsl.2020.116297

Rouxel, O., Shanks III, W. C., Bach, W., & Edwards, K. J. (2008). Integrated fe-and s-isotope study of seafloor hydrothermal vents at east pacific rise 9–10 n. *Chemical Geology*, *252*(3–4), 214–227. https://doi.org/10.1016/j.chemgeo.2008.03.009

Sarmiento, J. L., & Toggweiler, J. (1984). A new model for the role of the oceans in determining atmospheric p co2. *Nature*, *308*(5960), 621–624. https://doi.org/10.1038/308621a0

Scholz, F. S. S., McManus, J., Noffke, A., Lomnitz, U., & Hensen, C. (2014). On the isotope composition of reactive iron in marine sediments: Redox shuttle versus early diagenesis. *Chemical Geology*, *389*, 48–59. https://doi.org/10.1016/j.chemgeo.2014.09.009

Severmann, S., Johnson, C. M., Beard, B. L., German, C. R., Edmonds, H. N., Chiba, H., & Green, D. R. H. (2004). The effect of plume processes on the Fe isotope composition of hydrothermally derived Fe in the deep ocean as inferred from the Rainbow vent site, Mid-Atlantic Ridge, 36° 14′N. *Earth and Planetary Science Letters*, *225*(1), 63–76. https://doi.org/10.1016/j.epsl.2004.06.001

Severmann, S., Johnson, C. M., Beard, B. L., & McManus, J. (2006). The effect of early diagenesis on the Fe isotope compositions of porewaters and authigenic minerals in continental margin sediments. *Geochimica et Cosmochimica Acta*, *70*(8), 2006–2022. https://doi.org/10.1016/j.gca.2006.01.007

Severmann, S., McManus, J., Berelson, W. M., & Hammond, D. E. (2010). The continental shelf benthic iron flux and its isotope composition. *Geochimica et Cosmochimica Acta*, *74*(14), 3984–4004. https://doi.org/10.1016/j.gca.2010.04.022

Sieber, M., Conway, T. M., de Souza, G. F., Hassler, C. S., Ellwood, M. J., & Vance, D. (2021). Isotopic fingerprinting of biogeochemical processes and iron sources in the iron-limited surface southern ocean. *Earth and Planetary Science Letters*, *567*, 116967. https://doi.org/10.1016/j.epsl.2021.116967

Sieber, M., Lanning, N. T., Bian, X., Yang, S.-C., Takano, S., Sohrin, Y., et al. (2023). The importance of reversible scavenging for the marine Zn cycle evidenced by the distribution of zinc and its isotopes in the Pacific Ocean. *Journal of Geophysical Research: Oceans*, *128*(4), e2022JC019419. https://doi.org/10.1029/2022JC019419

Somes, C. J., Dale, A. W., Wallmann, K., Scholz, F., Yao, W., Oschlies, A., et al. (2021). Constraining global marine iron sources and ligand-mediated scavenging fluxes with geotraces dissolved iron measurements in an ocean biogeochemical model. *Global Biogeochemical Cycles*, *35*(8), e2021GB006948. https://doi.org/10.1029/2021gb006948

Staubwasser, M., Von Blanckenburg, F., & Schoenberg, R. (2006). Iron isotopes in the early marine diagenetic iron cycle. *Geology*, *34*(8), 629–632. https://doi.org/10.1130/g22647.1

Tagliabue, A., Aumont, O., DeAth, R., Dunne, J. P., Dutkiewicz, S., Galbraith, E., et al. (2016). How well do global ocean biogeochemistry models simulate dissolved iron distributions? *Global Biogeochemical Cycles*, *30*(2), 149–174. https://doi.org/10.1002/2015GB005289

Tagliabue, A., Bopp, L., Dutay, J.-C., Bowie, A. R., Chever, F., Jean-Baptiste, P., et al. (2010). Hydrothermal contribution to the oceanic dissolved iron inventory. *Nature Geoscience*, *3*(4), 252–256. https://doi.org/10.1038/ngeo818

Völker, C., & Ye, Y. (2022). Feedbacks between ocean productivity and organic iron complexation in reaction to changes in ocean iron supply. *Frontiers in Marine Science*, *9*. https://doi.org/10.3389/fmars.2022.777334

Waeles, M., Baker, A. R., Jickells, T., & Hoogewerff, J. (2007). Global dust teleconnections: Aerosol iron solubility and stable isotope composition. *Environmental Chemistry*, *4*(4), 233–237. https://doi.org/10.1071/en07013

Weber, T. S., John, S., Tagliabue, A., & DeVries, T. (2018). Biological uptake and reversible scavenging of zinc in the global ocean. *Science*, *361*(6397), 72–76. https://doi.org/10.1126/science.aap8532

Wehrmann, L. M., Formolo, M. J., Owens, J. D., Raiswell, R., Ferdelman, T. G., Riedinger, N., & Lyons, T. W. (2014). Iron and manganese speciation and cycling in glacially influenced high-latitude fjord sediments (West Spitsbergen, Svalbard): Evidence for a benthic recycling-transport mechanism. *Geochimica et Cosmochimica Acta*, *141*, 628–655. https://doi.org/10.1016/j.gca.2014.06.007

Windom, H. L., Moore, W. S., Niencheski, L. F. H., & Jahnke, R. A. (2006). Submarine groundwater discharge: A large, previously unrecognized source of dissolved iron to the south atlantic ocean. *Marine Chemistry*, *102*(3), 252–266. https://doi.org/10.1016/j.marchem.2006.06.016

Ye, Y. (2025a). Box model of the marine cycle of iron and iron isotopes [model code]. *Zenodo*. (Published: 2025-04-16). https://doi.org/10.5281/zenodo.15230278

Ye, Y. (2025b). Modelled fluxes of iron isotopes and collection of seawater iron isotope measurements from publications [Dataset]. *Zenodo*. (Published: 2025-03-14). https://doi.org/10.5281/zenodo.15017671

Zhang, R., Jensen, L., Fitzsimmons, J., Sherrell, R. M., Lam, P., Xiang, Y., & John, S. (2021). Iron isotope biogeochemical cycling in the western arctic ocean. *Global Biogeochemical Cycles*, *35*(11), e2021GB006977. https://doi.org/10.1029/2021GB006977